ADVANCED ELECTRONIC MATERIALS
www.advelectronicmat.de

Low Energy and Analog Memristor Enabled by Regulation of Ru ion Motion for High Precision Neuromorphic Computing

*Ji Eun Kim, Jae Uk Kwon, Suk Yeop Chun, Young Geun Song, Doo Seok Jeong, Chong-Yun Kang, Seong Keun Kim, Sahn Nahm, and Jung Ho Yoon**

Mobile species and matrix materials in ion motion-mediated memristors predominantly determine the switching characteristics and device performance. As a result of exploring a new type of mobile species, a Ru ion-mediated electrochemical metallization-like memristor with an amorphous oxide matrix is recently suggested to achieve a low switching current, voltage, and good retention simultaneously. Although the ion migration of Ru in the oxide matrix is previously confirmed, no in-depth study on how the crystallinity of the oxide matrix influences the Ru ion motion and switching characteristics has not been reported. Therefore, in this study, the crystallinity-dependent resistive switching behavior of the Pt/HfO_2/Ru structure device is investigated. With the crystallized HfO_2 layer, the preferred Ru ion migration through the grain boundaries occurs owing to the enhanced ion mobility, resulting in a high switching current (≈100 µA) with continuous metallic Ru conducting filaments. The discontinuous conducting filaments with amorphous HfO_2 exhibit a low switching current. In addition, highly linear and symmetric conductance modulation properties are achieved, and over 91.5% accuracy in the Mixed National Institute of Standards and Technology (MNIST) pattern recognition test is demonstrated.

1. Introduction

Modern computers are based on the von Neumann architecture and are intended to be general-purpose machines. This makes computers useful and convenient, however, they are highly ineffective for data-intensive tasks. To enhance the performance of computing systems in this "big data" era, we must transform the way we compute today towards a data-centric paradigm. Memristors or resistive switching (RS) devices are emerging candidates for next-generation data-driven computing applications such as neuromorphic computing,[1–5] physical computing,[6–8] and analog computing.[9–12] Although remarkable demonstrations for these applications have been reported recently,[13–18] an ideal memristor device that includes a low switching voltage, current, and good retention in the same device has not yet been successfully achieved. The switching characteristics of memristors significantly differ with regard to mobile species.[19–21] However, unfortunately, both low switching voltage and current with good retention are rarely observed in conventional oxygen vacancies-mediated valence change memory (VCM) or highly mobile cations-based electrochemical metallization (ECM). Owing to the relatively large activation energy (>1 eV) for oxide diffusion in the oxide matrix,[22] the VCM device exhibits either a low switching voltage or current, not both. In ECM devices, very low activation energy (<0.5 eV) for cations (e.g., Ag and Cu) in the electrolyte[23] induces poor retention even though the device can be operated with a low switching voltage and current. Therefore, a recent study revealed that Ru is a new type of mobile species with desirable switching properties.[24] The Ru ion-mediated ECM-like device has a median activation energy of ≈0.82 eV, at which the above important features can be implemented with a single device. Ru ions migrated via the amorphous Ta_2O_5 matrix and formed dispersed nanoclusters rather than continuous conducting filaments (CFs), exhibiting low on-current with good retention properties different from conventional Ag- or Cu-based ECM cells.[25–29] In this device, the amorphous Ta_2O_5 matrix might avoid making a preferred migration path, such as grain boundaries, which might enhance the Ru ion mobility and thereby induce continuous CFs. From that point of view, an investigation of the crystallinity-dependent RS characteristics of Ru-mediated ECM cells is necessary to confirm the influence of the matrix layer on these unique switching

J. E. Kim, J. U. Kwon, S. Y. Chun, Y. G. Song, C.-Y. Kang, S. K. Kim, J. H. Yoon
Electronic Materials Research Center
Korea Institute of Science and Technology (KIST)
Seoul 02791, Republic of Korea
E-mail: jhyoon@kist.re.kr
J. E. Kim, J. U. Kwon, S. Nahm
Department of Materials Science and Engineering
Korea University
Seoul 02841, Republic of Korea
S. Y. Chun, C.-Y. Kang, S. K. Kim, S. Nahm
KU-KIST Graduate School of Converging Science and Technology
Korea University
Seoul 02841, Republic of Korea
D. S. Jeong
Division of Materials Science and Engineering
Hanyang University
Seoul 04763, Republic of Korea

The ORCID identification number(s) for the author(s) of this article can be found under https://doi.org/10.1002/aelm.202200365.

DOI: 10.1002/aelm.202200365

characteristics. This will further help to optimize the device to achieve desirable switching characteristics.

Therefore, this study investigated the crystallinity-dependent RS behavior of the Pt/HfO_2/Ru structure. We observed that a Ru memristor (Pt/HfO_2/Ru) with an amorphous HfO_2 layer can switch at a low current (≈1 µA) and exhibit a gradual current change. Otherwise, with a crystalline HfO_2 layer, the on-current reaches ≈100 µA after the set process with the same compliance current (I_{cc}) of 1 µA, and an abrupt current change is observed, same as in conventional ECM cells, with the only difference being the crystallinity. Therefore, it is believed that the critical factor that determines either high or low on-current is the presence or absence of preferential migration paths, which are grain boundaries that grant high mobility and low activation energy for ion diffusion.[30–32] Such differences result in the formation of continuous and non-continuous CFs with crystalline and amorphous HfO_2, respectively. Notably, non-continuous CFs could induce highly linear and symmetric conductance modulation properties, achieving maximum simulated inference accuracies of >90% in the Mixed National Institute of Standards and Technology (MNIST) pattern recognition test. Such crystallinity-dependent switching and fine conductance modulation properties are investigated and discussed together with a reasonable model based on detailed physical characterizations and electrical measurements of the devices.

2. Results and Discussion

The Ru memristor was composed of a Pt TE/5 nm-thick-HfO_2/Ru BE stack structure with a 10 × 10 µm cross-bar configuration (see Experimental Section). **Figure 1**A presents the *I–V* curves of the as-fabricated Ru memristor device, including the set and reset switching, indicated by dashed arrows. The electrical bias is commonly applied to the TE, while the BE is grounded for the DC and pulse measurements. The set switching with an I_{cc} of 1 µA was induced at approximately −1.3 V. The maximum current of the on state (low resistance state, LRS) was ≈1 µA. During the reset switching, the on-current gradually decreased to the off state from 1 V, and the state is completely switched back to its off state (high resistance state, HRS) with a reset voltage of approximately 2.8 V. This unique low-energy RS is almost identical to the previous result observed in the Pt/Ta_2O_5/Ru structure device,[24] which was rarely reported in either VCM or ECM devices with a HfO_2 switching layer.[19,33] Figure 1B shows the RS *I–V* curves of the Ru memristor annealed at 500 °C for 1 min in an Ar atmosphere, exhibiting significantly different RS behavior compared with the as-fabricated device. Although the applied I_{cc} is 1 µA, the maximum on-current increases to ≈100 µA, which is almost two orders of magnitude higher than that of the as-fabricated device (≈1 µA). During the reset operation, the current abruptly dropped from the on to the off state at around 0.7 V and showed a subsequent gradual current change to the off state. This RS behavior highly resembles the conventional ECM switching behavior,[19] implying that continuous CFs might be formed even though the set switching was induced by the smaller set voltage of −1 V and the same I_{cc} condition. To determine the reason for these apparent differences in the switching characteristics of the as-fabricated and annealed Ru memristors, the structural and crystallographic features were investigated. Figure 1C shows the X-ray diffraction (XRD) patterns of the as-deposited and annealed HfO_2 films. In the as-fabricated device, there is no diffraction peak corresponding to the crystalline phases of HfO_2, whereas the monoclinic HfO_2 peaks appear in the annealed device. Figure 1D,E present the cross-sectional high-resolution transmission electron microscopy (HRTEM) images of the as-fabricated and annealed Ru memristors, respectively. Compared with the as-fabricated structure, where the lattice fringes are not visible (Figure 1D), the lattice fringes in the 5 nm-thick HfO_2 layer are clearly seen in the annealed device, which is consistent with the XRD pattern data. Figure 1E-ii shows two distinct lattice arrangements indexed as regions I and II. As shown in Figure 1E(i,iii), the diffraction patterns obtained by fast Fourier transform (FFT) in regions I and II indicate the formation of the monoclinic phase HfO_2 with different orientations, revealing that the grain boundary vertical to the BE and TE is located between the two columnar grains.

Such a drastic change in the RS behavior with and without the annealing process was considered to be related to the presence and absence of grain boundaries, which were previously studied as preferred ion migration paths due to the lower activation energy for ion diffusion.[30–32] Therefore, both the as-fabricated and annealed devices were examined using conductive atomic force microscopy (CAFM) by focusing on the distribution of locally hollowed regions and conducting spots upon crystallization. CAFM was conducted before depositing the top Pt electrode. The AFM tip was negatively biased at −7 V during the measurement, and the bottom Ru electrode was grounded. The topographic image in Figure S1, Supplementary Information shows the crystallization of the HfO_2 layer after annealing. **Figure 2**A,B show the overlapped topographic and current images of the as-fabricated and annealed devices. For the as-fabricated device, a small number of conducting spots were randomly dispersed over the entire HfO_2 surface, while in the annealed device, the conducting spots are localized along the hollowed regions, supposedly grain boundaries, implying the formation of conducting paths through grain boundaries. The line profiles of the topographic and current images of the as-fabricated and annealed devices further confirm these tendencies, as shown in Figure 2C,D, respectively, obtained from the dotted line in Figure 2A,B. The conducting spots in the as-fabricated device are located randomly, regardless of the relative height of the HfO_2 surface with an output current of ≈30 nA. In contrast, conducting spots are locally formed in the hollowed region of the annealed HfO_2 surface with a higher current of ≈70 nA. These results imply that relatively strong CFs were formed via the grain boundaries because of the preferred migration of Ru ions in the annealed device,[31] whereas weak CFs were randomly formed in the as-fabricated device.

To further understand the configuration of CFs in the as-fabricated and annealed devices, conduction mechanism analysis for the on state was conducted by measuring the temperature-dependent *I–V* curves. **Figure 3**A,B shows the temperature-dependent *I–V* curves of the as-fabricated (70–100 °C) and annealed (50–250 °C) devices in the on-state, respectively. The on-state was obtained by a set operation with an I_{cc} of 1 µA. In the as-fabricated device, the *I–V* curve does not show any temperature dependence (Figure 3A). The inset in Figure 3A presents log *I* versus log *V* curves with a slope of ≈1, implying that

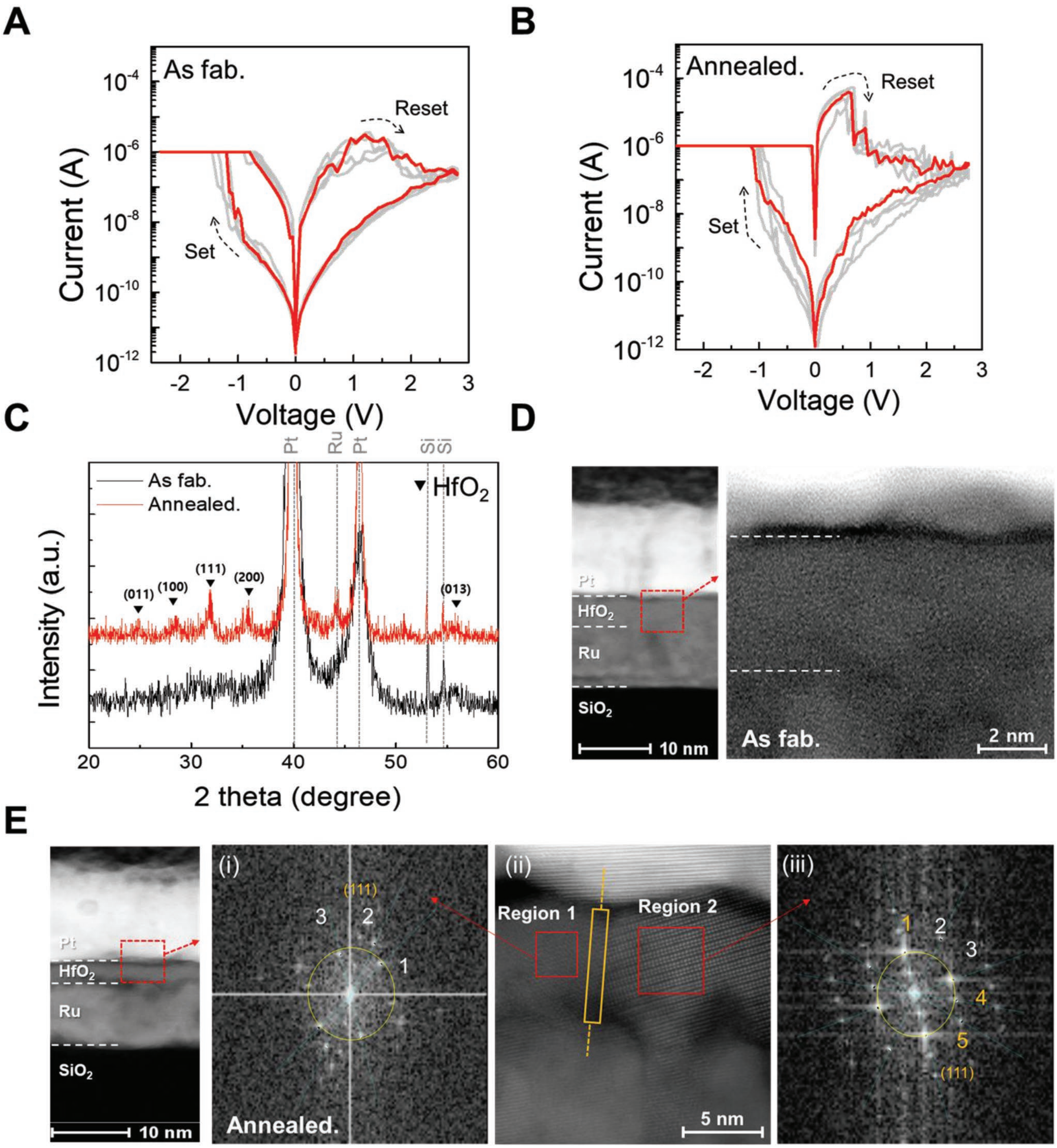

Figure 1. Resistive switching *I–V* curves of the A) as-fabricated and B) annealed Pt/HfO_2 5 nm/Ru device. C) XRD pattern of as-fabricated and annealed HfO_2. Cross-sectional dark-field STEM images of the D) as-fabricated and E) annealed Pt/HfO_2/Ru device. E) Cross-sectional HR-TEM image of the annealed Pt/HfO_2/Ru device with lattice fringes and FFT patterns. The FFT patterns of i) and iii) correspond to the dotted squares in (ii).

the tunneling conduction mechanism dominates the current conduction. Similar to a previous report,[24] in the as-fabricated device, the formed CFs might not be in the form of continuous CFs, but in the form of discrete nanoclusters in the HfO_2 layer. Otherwise, for the annealed device, the current decreased with increasing temperature (Figure 3B), suggesting the formation of continuous metallic CFs. To carefully check the composition of the CFs, the thermal coefficient of the metallic CFs was measured. The thermal coefficient for CFs is ≈3.6×10^{-4} extracted from the $(R - R_{393K})/R_{393K}$ versus T graph in the inset of Figure 3B, which is quite similar to the value of Ru BE (≈4.15×10^{-4}), indicating that the continuous metallic CFs consist of Ru. The extracted thermal coefficient of Ru BE is relatively smaller than the reported value of bulk Ru (≈4×10^{-3}),[34,35]

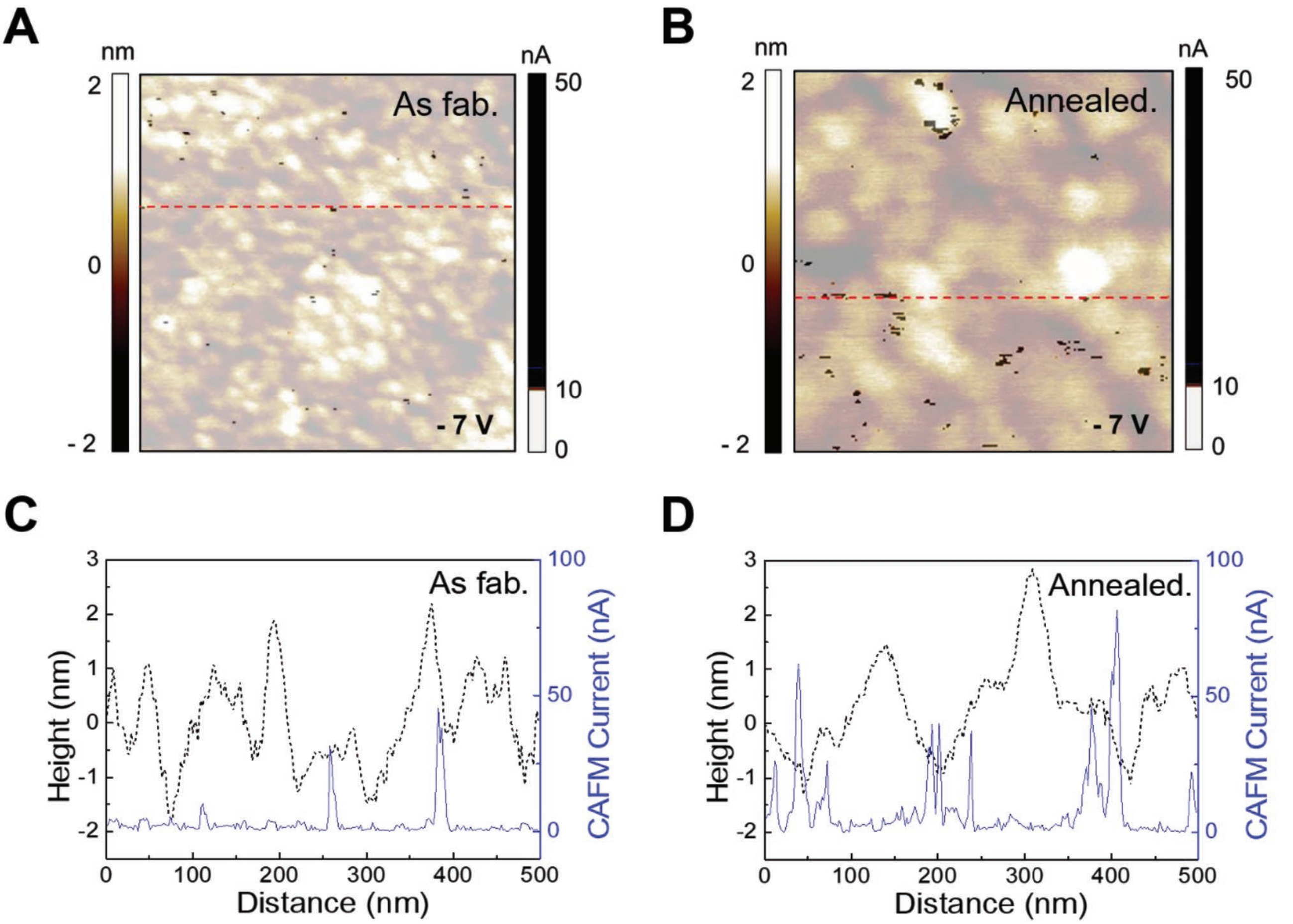

Figure 2. The digitized topographic and current images of the A) as-fabricated and B) annealed HfO_2/Ru. Line profile of the topographic and current images (marked by the red dotted lines in [A,B]) of C) as-fabricated and D) annealed HfO_2/Ru.

which is consistent with previous studies showing that the temperature coefficient of a metallic thin film is typically smaller than that of the bulk material. Figure 3C,D illustrate the plausible circumstances of the as-fabricated and annealed devices in the on state. The discrete Ru nanoclusters were randomly dispersed after the set operation in the as-fabricated device. With the low I_{cc} in the set process, due to the high activation energy for migration and low mobility of Ru ions in the amorphous HfO_2 matrix, the Ru supply is insufficient to form continuous CFs, and thus the migrated Ru is dispersed in the form of nanoclusters in the HfO_2 layer. Therefore, these nanoclusters can act as tunneling sites for electrons injected from the BE, enabling the unique low on-current RS behavior. In the annealed device, the set voltage (–1 V) was slightly lower than that of the as-fabricated device (–1.3 V), as shown in Figure 1A,B, revealing the smooth and preferential migration of Ru ions with low activation energy through grain boundaries in the annealed device. In addition, the high on-current and metallic conduction in the on state confirmed the formation of continuous CFs. These results reveal that the amorphous oxide is a prerequisite for inducing relatively high activation energy for Ru ion migration. Therefore, in addition to adopting Ru as a mobile species, employing an appropriate oxide layer that can avoid forming strong and continuous CFs is essential for achieving a unique low-current switching. To further check whether the annealing process itself affects the RS of the Ru memristor, as-fabricated and annealed Ru memristors with the Pt/Ta_2O_5/Ru structures were prepared using the same experimental procedure as the Pt/HfO_2/Ru device, except for the Ta_2O_5 layer. Since the reported crystallization temperature for Ta_2O_5 is approximately 750 °C,[36,37] Ta_2O_5 remains amorphous after an identical annealing step at 500 °C for the annealed HfO_2-based Ru memristor, as confirmed by the XRD results shown in Figure S2A, Supplementary Information. Figure S2B,C, Supplementary Information show almost identical RS *I–V* curves of the as-fabricated and annealed Ta_2O_5-based Ru memristor, respectively, implying that the annealing step without the crystallization of the oxide layer does not induce a drastic change in the RS behavior.

Figure 4 shows the performances, such as switching speed, retention, and endurance, of the as-fabricated device. The upper panel of Figure 4A shows a train of input voltage pulses for the pre-read (+0.5 V, 500 µs), set (–3 V, 50 ns), read (+0.5 V, 500 µs), reset (+3 V, 50 ns), and read again (+0.5 V, 500 µs) operations. The lower panel of Figure 4A shows the output currents according to the train of input voltage pulses, revealing that the device successfully switched from the off to the on state and vice versa with 50 ns set and reset pulses. The

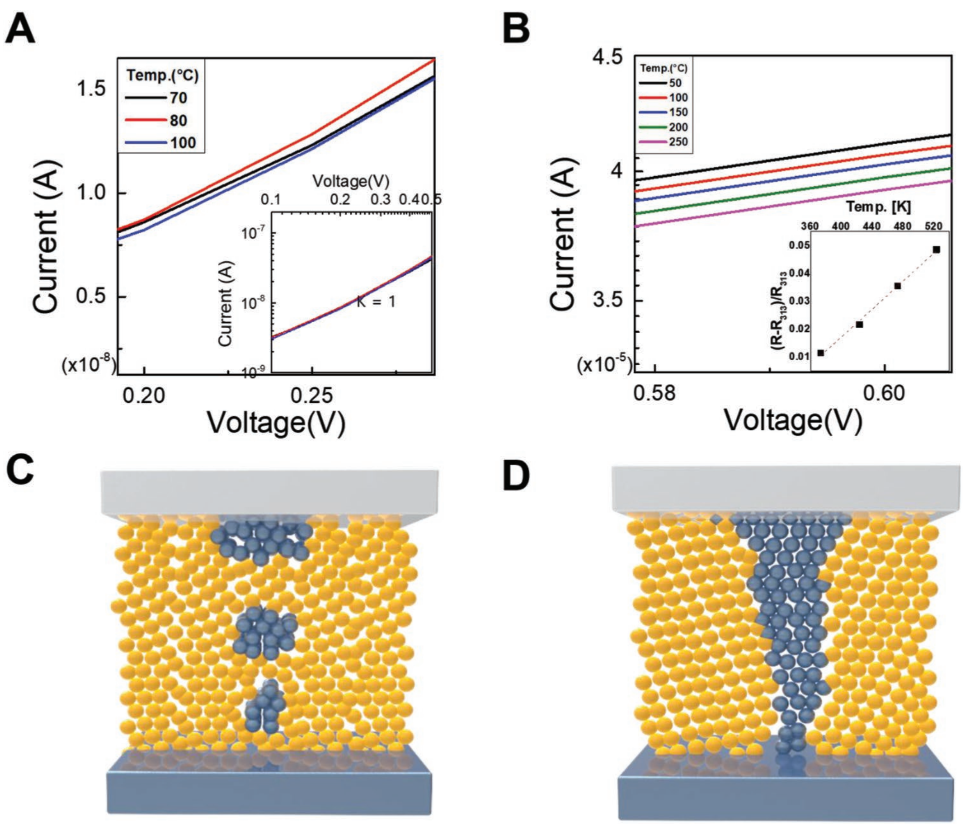

Figure 3. A) *I–V* curves in the LRS of the as-fabricated Pt/HfO_2/Ru. Inset figure of (A) shows the log *I*–log *V* curves with a slope of ≈1. B) *I–V* curves in the LRS of the annealed Pt/HfO_2/Ru. Inset figure of (B) shows the $(R - R_{393K})/R_{393K}$ versus *T*. Schematic diagrams illustrating the distributions of Ru ions in C) as-fabricated and D) annealed Pt/HfO_2/Ru.

device retention in the on state was measured at different temperatures ranging from 160 to 250 °C, as shown in the inset of Figure 4B. The retention property of the off state was measured at 250 °C; however, there was no noticeable change up to 10^4 s, indicating that the HRS is less of a concern than the on state. For the retention characterization, the resistance was measured with an interval time of 10 s at –0.5 V. The current drops were observed in the on state at a certain time at these elevated temperatures. The particular time when the sudden decrease in current from the on state was collected as the retention time at each temperature. The data were re-plotted in the form of retention time versus $1/(kT)^{-1}$ graph to estimate the retention time at RT. As shown in Figure 4B, the expected retention time was approximately 2 years at RT. In addition, the current values in various intermediate states obtained by adjusting the reset voltage ranging from 1 to 2.8 V (fully off) during reset switching show a narrow distribution and no degradation for 1000 s at 95 °C, as shown in Figure S3, Supplementary Information, revealing its good retention properties. Figure 4C shows the resistance values read at 0.5 V for the on and off states extracted from 1000 repeated DC sweep cycle tests at 95 °C. The resistance values in both on and off states show very narrow distributions, and the on/off ratio is larger than 100 and is maintained within continuous DC operation, confirming its good cycle-to-cycle uniformity. The almost identical switching *I–V* curves obtained from 10 different devices shown in Figure S4, Supplementary Information further confirm its good device-to-device uniformity. Figure S5, Supplementary Information shows the non-area-dependency of the on and off state of the as-fabricated device. The device size does not affect the switching characteristics, implying another merit in terms of device scaling. In addition to these RS performances, analog switching capability has attracted significant attention as the most important characteristic for emerging analog computing applications. Recent remarkable demonstrations confirmed that highly linear and symmetric conductance modulation is the most crucial factor for achieving high-precision synaptic weight representations.[1,3,38,39] Therefore, the conductance modulation properties of the as-fabricated and annealed Ru memristors were measured. **Figure 5**A,B show the conductance modulation and its variation in the as-fabricated and annealed Ru memristors, respectively, measured by identical pulse trains repeated three times. The as-fabricated device was measured using potentiation and depression pulses with amplitudes of –1.5 and 2.3 V, respectively, and a pulse width of 200 ns, exhibiting highly linear and symmetric conductance changes. To evaluate the linearity of the conductance modulation, the linearity was calculated using the concepts defined by Equations (1) and (2):

$$\text{Linearity factor} = \frac{\dfrac{\Delta G_{\max} + \Delta G_{\min}}{2}}{\dfrac{G_{\max} - G_{\min}}{\text{pulse number}}} \quad (1)$$

ADVANCED ELECTRONIC MATERIALS
www.advelectronicmat.de

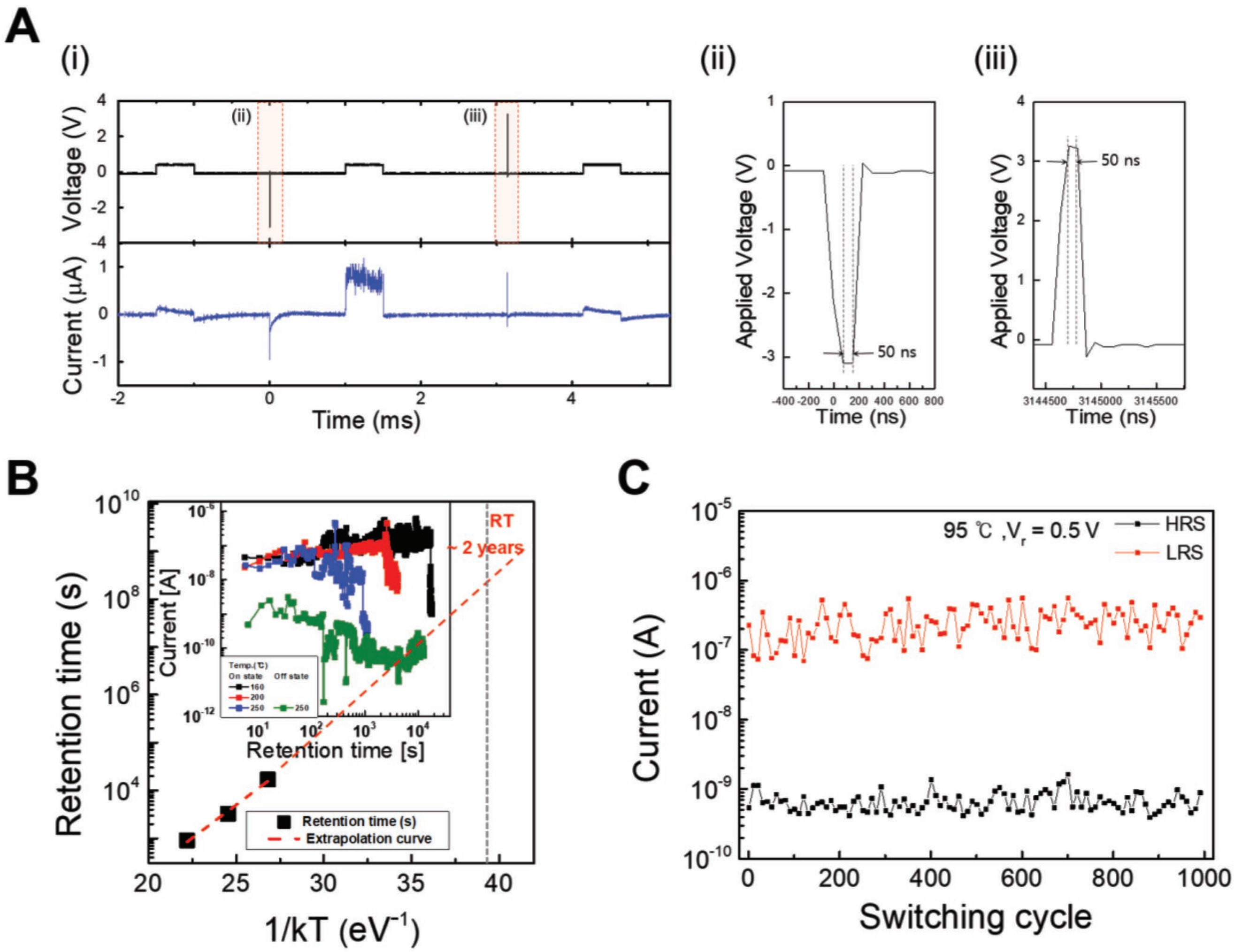

Figure 4. A) Pulse switching characteristics of the device. The upper panel of i) is a set of input voltage pulses for read (+0.5 V), set (–3 V), read (+0.5 V), reset (+3 V), and read again (+0.5 V) operations, with a set and reset pulse width of 50 ns and read pulse width of 500 µs, and the lower panel of the current readings of the device corresponding to the input voltage pulses. (ii) and (iii) are zoomed-in set and reset pulse. B) Retention time versus $1/(kT)^{-1}$ graph (time-failure graph) and (inset to (B) retention time of LRS and HRS at different temperatures ranging from 160 to 250 °C. C) Endurance data measured up to 1000 cycles at 95 °C.

$$\text{Symmetry factor} = \max\left(\frac{\Delta G_D}{\Delta G_P}, \frac{\Delta G_P}{\Delta G_D}\right) \quad (2)$$

where ΔG_{min} and ΔG_{max} are the minimum and maximum changes in conductance between neighboring values, and ΔG_D and ΔG_P are the total conductance changes, as reported in a previous study.[38] The calculated linearity of potentiation (α_p) and depression (α_d) are ≈1.01 and ≈1.36, respectively, and the symmetry is ≈1.01, which has been rarely achieved in conventional two-terminal memristor devices.[40–43] In addition, the overlapped conductance modulation curves with repeated three consecutive measurements represent a highly uniform and reliable conductance change in the as-fabricated device. The potentiation and depression of the annealed device were measured by applying –1 and 2.5 V with a width of 200 ns. Unlike the as-fabricated device, an abrupt conductance change appears for both the potentiation and depression operations (see the red-colored region in Figure 5B), resulting in large α_p and α_d values of 9.96 and 9.37, respectively, and symmetry of ≈1.15. These sudden conductance changes are randomly induced regardless of the accumulated pulse inputs, hindering high-precision learning and inferences. The conductance changes in the red-colored region, where the abrupt conductance jump (drop) is shown, is over 60% of the total amount of the conductance change, revealing that the number of allocable conductance states is significantly less with the same memory window in the annealed device. For the annealed device, the Ru ions can move easily via the grain boundaries, so that a larger gradual conductance change is induced until the CFs connect to the counter electrode. After that, a sudden conductance jump was observed with the completion of the CF growth. Similarly, during the subsequent depression operation, a sudden conductance drop is observed because of the disconnection of CFs as Ru ions move back to BE. Otherwise, in the as-fabricated device, owing to the low ion mobility and high activation energy for Ru ion diffusion, the Ru ion supply is restricted; thus, the amount of change in

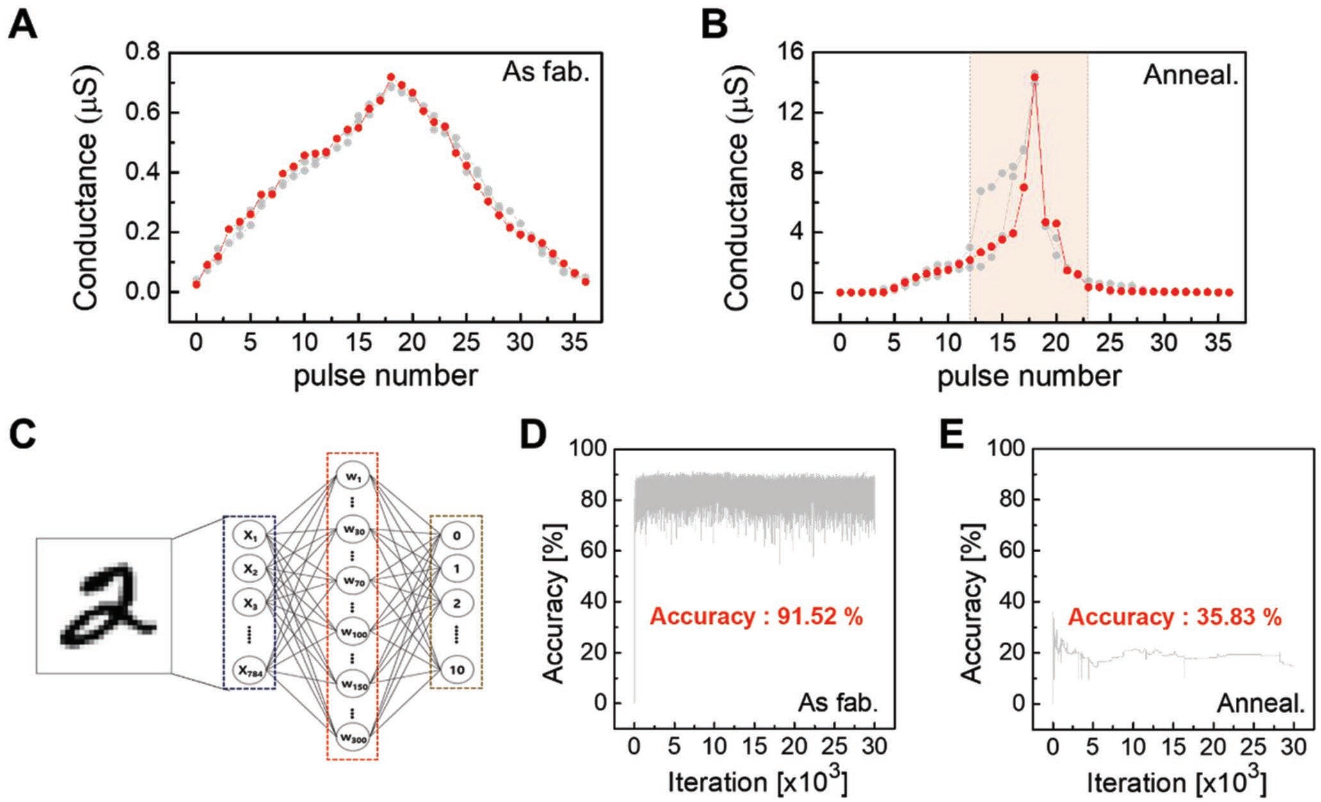

Figure 5. Conductance modulation and its variation in the A) as-fabricated and B) annealed Pt/HfO_2/Ru device measured by identical pulse trains repeated three times. C) Schematic structure of MNIST-based inference simulation system. 784 300, and 10 nodes were placed in the input, hidden, and output layers, respectively. Simulation results of inference accuracy of the D) as-fabricated and E) annealed device, respectively. In the case of the as-fabricated device, an inference accuracy of up to 91.52% was estimated, whereas the annealed device exhibited an inference accuracy of 35.83% and a relatively large fluctuation.

conductance per input pulse is smaller than that observed in the annealed device. Potentiation pulses induce the migration of Ru from BE to the HfO_2 oxide, which increases the tunneling sites and decreases the tunneling distance between each tunneling site, resulting in an increase in conductance. As the subsequent depression pulses are applied, Ru ions move back to the BE, gradually decreasing the conductance. To demonstrate the superior performance of the as-fabricated Ru memristor, which has highly linear and symmetric conductance modulation properties, the soft-based neural network simulation for MNIST pattern recognition was conducted. The MNIST dataset (images of handwritten digits with a pixel resolution of 28 × 28, each with an 8-bit grayscale value) was used as a test vector, including 60 000 training data and 10 000 validation data. The simulation included one hidden layer containing 300 nodes, an input layer (784 nodes), and an output layer (10 nodes),[44] as depicted in Figure 5C. Figure 5D,E show the maximum inference accuracies of ≈91.52% and ≈35.83% using the representative curves in Figure 5A,B of the as-fabricated and annealed devices, respectively. The annealed device exhibits a larger fluctuation in the simulation result than the as-fabricated device owing to its worse linearity. Because the back-propagation algorithm is used to evaluate the weight change, this algorithm presumes a linear change in conductance to determine the number of optimal programming pulses for the weight update. Thus, when the linearity is poor, the number of programming pulses applied for a target weight change is miscalculated. In addition, the non-uniformity and large variations of the change in conductance in repeated measurements can cause further degradation of the inference accuracy.

3. Conclusion

In summary, the crystallinity-dependent RS properties of a Ru-ion-mediated memristor device with a Pt/HfO_2/Ru stack structure were investigated. The annealing process crystallized the amorphous HfO_2 layer in the as-fabricated Ru memristor, and the HRTEM and XRD results indicated the formation of columnar grains with grain boundaries between them. The preferential migration of Ru ions in the crystalline HfO_2 layer was confirmed via the CAFM study, revealing that the Ru ion mobility is enhanced owing to the lower activation energy for diffusion through the grain boundaries. From the carefully conducted conduction mechanism analysis of the as-fabricated and annealed devices, it was confirmed that continuous metallic Ru CFs were formed at the grain boundaries in the annealed devices, whereas the non-continuous CFs, which consisted of Ru (or RuO_x) nanoclusters in the as-fabricated Ru memristor, induced a low on-state due to the tunneling conduction. In addition, the annealing process without crystallization in Pt/Ta_2O_5/Ru does not significantly affect the RS characteristics, suggesting that the crystallinity of the matrix materials is a significant factor in inducing low current switching behavior. It is worth noting that highly linear and symmetric conduction modulation properties were obtained in the as-fabricated Ru memristor, which might be attributed to the restriction of Ru supply during switching operations, resulting in a smaller change in conductance and avoiding an abrupt change, which is observed in the annealed Ru memristors. Using the as-fabricated Ru memristor, high accuracy of over 91.5% in the MNIST pattern recognition simulation was achieved, implying its potential for use in analog and neuromorphic computing applications.

4. Experimental Section

Device Fabrication: A cross-point memristor device with an area of 10×10 µm was fabricated using conventional photolithography and lift-off steps. The structure consists of a 5 nm-thick amorphous HfO_2 layer sandwiched between a 30 nm-thick Ru (bottom electrode, BE) and a 30 nm-thick Pt (top electrode, TE) layer. The bottom Ru electrode was deposited using a direct-current (DC) sputtering system on a SiO_2/Si substrate. The switching matrix, HfO_2, was grown by atomic layer deposition (ALD) at 260 °C using tetrakis (ethylmethylamino) hafnium (TEMAH) and ozone (O_3) as precursors for Hf and O, respectively. Next, the top Pt electrode was sputtered on top of the HfO_2 layer. Subsequently, the device was annealed at 500 °C for 1 min in an Ar atmosphere using rapid thermal annealing (RTA) system for the crystallization of the HfO_2 layer.

Characterization: Cross-sectional TEM (Titan) was used to analyze the structure of the material. The TEM specimens were prepared using a focused ion beam (FIB, Hitachi-NX5000). The crystallinity of the HfO_2 layer was investigated by glancing angle XRD (D8 Advance) and high-resolution cross-sectional TEM. Atomic force microscopy (CAFM, XE-100) was performed in contact mode to correlate the morphology and localize the electrical conduction paths of the HfO_2 layer. The RS performance was measured using a semiconductor parameter analyzer (HP 4155A) under ambient conditions. An oscilloscope (DSO-X 3014A) and a pulse generator unit (AFG-3102C) were used for pulse measurements. Electrical bias was commonly applied to the TE for electrical measurements, while the BE was grounded.

Evaluation of the Inference Accuracy: The MNIST database is a huge database that is often used for machine learning training and testing.[44] Each potentiation and depression characteristic was examined with consecutive 18 negative and 18 positive pulses. Both behaviors were modeled using $G(n) = A + Be^{-Cn}$, where the pulse index n was evaluated before the weight update for each epoch. The experimentally acquired data were curve fitted and used to obtain the ideal parameters A, B, and C. The weight w was converted from the conductance of the device and expressed as $w = (G - G_{mean})/G_{diff}$, where $G_{mean} = [G_P(0) + G_D(0)]/2$, and $G_{diff} = G_D(0) - G_P(0)$. A detailed description of the training algorithm in this study is presented in a previous study.[38]

Supporting Information

Supporting Information is available from the Wiley Online Library or from the author.

Acknowledgements

This work was supported by National R&D Program through the National Research Foundation of Korea (NRF) funded by Ministry of Science and ICT (NRF-2021M3F3A2A01037738 and NRF-2022R1C1C1004176), and the Korea Institute of Science and Technology (2E31771 and 2V09333).

Conflict of Interest

The authors declare no conflict of interest.

Data Availability Statement

The data that support the findings of this study are available from the corresponding author upon reasonable request.

Keywords

analog switching, conductance modulation, crystallinity-dependent, low currents, memristors

Received: March 31, 2022
Revised: May 11, 2022
Published online:

[1] S. Choi, J. Yang, G. Wang, *Adv. Mater.* **2020**, *32*, 2004659.
[2] N. K. Upadhyay, H. Jiang, Z. Wang, S. Asapu, Q. Xia, J. Joshua Yang, *Adv. Mater. Technol.* **2019**, *4*, 1800589.
[3] V. K. Sangwan, M. C. Hersam, *Nat. Nanotechnol.* **2020**, *15*, 517.
[4] H. Li, S. Wang, X. Zhang, W. Wang, R. Yang, Z. Sun, W. Feng, P. Lin, Z. Wang, L. Sun, Y. Yao, *Adv. Intell. Syst.* **2021**, *3*, 2100017.
[5] W. Banerjee, *Electronics* **2020**, *9*, 1029.
[6] D. S. Jeong, K. M. Kim, S. Kim, B. J. Choi, C. S. Hwang, *Adv. Electron. Mater.* **2016**, *2*.
[7] A. Mehonic, A. Sebastian, B. Rajendran, O. Simeone, E. Vasilaki, A. J. Kenyon, *Adv. Intell. Syst.* **2020**, *2*, 2000085.
[8] D. Ielmini, S. Ambrogio, *Nanotechnology* **2020**, *31*, 092001.
[9] Y. Xi, B. Gao, J. Tang, A. Chen, M.-F. Chang, X. S. Hu, J. V. D. Spiegel, H. Qian, H. Wu, *Proc. IEEE* **2021**, *109*, 14.
[10] T. Shi, R. Wang, Z. Wu, Y. Sun, J. An, Q. Liu, *Small Struct.* **2021**, *2*, 2170010.
[11] M. Hu, C. E. Graves, C. Li, Y. Li, N. Ge, E. Montgomery, N. Davila, H. Jiang, R. S. Williams, J. J. Yang, Q. Xia, J. P. Strachan, *Adv. Mater.* **2018**, *30*, 1705914.
[12] M. Zhao, B. Gao, J. Tang, H. Qian, H. Wu, *Appl. Phys. Rev.* **2020**, *7*, 011301.
[13] C. H. Cheng, C. Y. Tsai, A. Chin, F. S. Yeh, in *IEEE 2010 IEEE Int. Electron Devices Meeting (IEDM)*, San Francisco, CA, USA **2010**, p. 19.
[14] W. Banerjee, R. D. Nikam, H. Hwang, *Appl. Phys. Lett.* **2022**, *120*, 060501.
[15] A. Fantini, L. Goux, R. Degraeve, in *5th IEEE Int. Memory Workshop (IMV)*, **2013**, pp. 30–33.
[16] W. Banerjee, S. H. Kim, S. Lee, S. Lee, D. Lee, H. Hwang, *Adv. Funct. Mater.* **2021**, *31*, 2104054.
[17] W. Banerjee, W. F. Cai, X. Zhao, Q. Liu, H. Lv, S. Long, M. Liu, *Nanoscale* **2017**, *9*, 18908.
[18] W. Banerjee, S. Z. Rahaman, A. Prakash, S. Maikap, *Jpn. J. Appl. Phys.* **2011**, *50*, 10PH01.
[19] I. Valov, R. Waser, J. R. Jameson, M. N. Kozicki, *Nanotechnology* **2011**, *22*, 289502.
[20] C. Ye, J. Wu, G. He, J. Zhang, T. Deng, P. He, H. Wang, *J. Mater. Sci. Technol.* **2016**, *32*, 1.
[21] R. Waser, R. Dittmann, G. Staikov, K. Szot, *Adv. Mater.* **2009**, *21*, 2632.
[22] R. Nakamura, T. Toda, S. Tsukui, M. Tane, M. Ishimaru, T. Suzuki, H. Nakajima, *J. Appl. Phys.* **2014**, *116*, 033504.
[23] P. Boolchand, W. Bresser, *Nature* **2001**, *410*, 1070.
[24] J. H. Yoon, J. Zhang, P. Lin, N. Upadhyay, P. Yan, Y. Liu, Q. Xia, J. J. Yang, *Adv. Mater.* **2020**, *32*, 1904599.

ADVANCED ELECTRONIC MATERIALS
www.advelectronicmat.de

[25] M. Saadi, P. Gonon, C. Vallée, F. Jomni, E. Jalaguier, A. Bsiesy, *J. Mater. Sci.: Mater. Electron.* **2020**, *31*, 13487.
[26] Z. Wang, M. Rao, R. Midya, S. Joshi, H. Jiang, P. Lin, W. Song, S. Asapu, Y. Zhuo, C. Li, H. Wu, Q. Xia, J. J. Yang, *Adv. Funct. Mater.* **2017**, *28*,
[27] M. Zhang, S. Long, Y. Li, Q. Liu, H. Lv, E. Miranda, J. Sune, M. Liu, *Nanoscale Res. Lett.* **2016**, *11*, 269.
[28] Y. Yang, P. Gao, S. Gaba, T. Chang, X. Pan, W. Lu, *Nat. Commun.* **2012**, *3*, 732.
[29] H. Lv, Xu, X. , Liu, H. , Luo, Q. , Liu, Q. , Long, S. , Liu, M. , in *IEEE Int. Conf. on Electron Devices and Solid-State Circuits (EDSSC),* Singapore, June **2015**, p. 229.
[30] R. D. Kamachali, *RSC Adv.* **2020**, *10*, 26728.
[31] M. Lanza, *Materials* **2014**, *7*, 2155.
[32] R. Balluffi, *Metall. Trans. B* **1982**, *13*, 527.
[33] Z. Shen, C. Zhao, Y. Qi, W. Xu, Y. Liu, I. Z. Mitrovic, L. Yang, C. Zhao, *Nanomaterials* **2020**, *10*, 1437.
[34] R. B. Belser, W. H. Hicklin, *J. Appl. Phys.* **1959**, *30*, 313.
[35] F. Warkusz, *J. Phys. D: Appl. Phys.* **1978**, *11*, 689.
[36] S. Ezhilvalavan, T.-Y. Tseng, *J. Mater. Sci.: Mater. Electron.* **1999**, *10*, 9.
[37] A. Pignolet, G. M. Rao, S. Krupanidhi, *Thin Solid Films* **1995**, *258*, 230.
[38] J. J. Ryu, K. Jeon, G. Kim, M. K. Yang, C. Kim, D. S. Jeong, G. H. Kim, *Adv. Electron. Mater.* **2020**, *6*, 2000434.
[39] Z. Wang, H. Wu, G. W. Burr, C. S. Hwang, K. L. Wang, Q. Xia, J. J. Yang, *Nat. Rev. Mater.* **2020**, *5*, 173.
[40] J.-U. Woo, H.-G. Hwang, S.-M. Park, T.-G. Lee, S. Nahm, *Appl. Mater. Today* **2020**, *19*, 100582.
[41] S. Y. Min, W. J. Cho, *Int. J. Mol. Sci.* **2021**, *22*, 773.
[42] K. Yin, M. Li, Y. Liu, C. He, F. Zhuge, B. Chen, W. Lu, X. Pan, R.-W. Li, *Appl. Phys. Lett.* **2010**, *97*, 042101.
[43] X. Yan, L. Zhang, H. Chen, X. Li, J. Wang, Q. Liu, C. Lu, J. Chen, H. Wu, P. Zhou, *Adv. Funct. Mater.* **2018**, *28*, 1803728.
[44] The MNIST Database of Handwritten Digits, http://yann.lecun.com/exdb/mnist/ (accessed: 1998).